PHYSICAL REVIEW RESEARCH **7**, 033056 (2025)

Probing the hollowing transition of a shell-shaped Bose-Einstein condensate with collective excitation

Zerong Huang,[1,*] Kai Yuen Lee,[1,*] Chun Kit Wong,[1,†] Liyuan Qiu,[1] Bo Yang,[1,‡]
Yangqian Yan,[1,2] and Dajun Wang[1,2,§]
[1]*Department of Physics, The Chinese University of Hong Kong, Hong Kong SAR, China*
[2]*State Key Laboratory of Quantum Information Technologies and Materials, The Chinese University of Hong Kong, Hong Kong SAR, China*

(Received 26 February 2025; accepted 2 June 2025; published 14 July 2025)

We investigate the hollowing transition of a shell-shaped Bose-Einstein condensate using collective excitations. The shell is created using an immiscible dual-species Bose-Einstein condensate mixture, with its hollowness controlled by tuning the repulsive interspecies interaction via a Feshbach resonance. Our results reveal two distinct monopole modes in which the two condensates oscillate either in phase or out of phase. The spectrum of the out-of-phase mode exhibits a nonmonotonic dependence on the interspecies interaction, providing a clear signature of the topology change from a filled to a hollow condensate. Furthermore, we find that the critical point of the hollowing transition depends strongly on the number ratio of the two species. Our findings provide a detailed understanding of the topology change in shell-shaped quantum gases and pave the way for future study of quantum many-body phenomena in curved spaces.

DOI: 10.1103/dbm1-7dy4

I. INTRODUCTION

The study of double-species Bose-Einstein condensates (BECs) dates back to 1957 [1], when the superfluid helium mixture was theoretically studied for the first time. Following the creation of BECs of dilute atomic gases in 1995, interest in this topic was revived, leading to intense theoretical and experimental explorations still ongoing to date. Although earlier studies primarily focused on phase separation, that is, the miscible-immiscible transition for repulsive intraspecies and interspecies interactions [2–17], the recent discovery of the quantum liquid droplet phase in the mean field collapsing regime [18–22] demonstrates that there remains a wealth of physics to explore in the dual-species BEC system.

Previous experimental studies of the miscible-immiscible transition have predominantly been conducted in elongated traps [10,12,15,23]. In such geometries, the phase separation largely resembles a smeared-out version of the transition in free space, with the critical scattering length (a_c) only slightly shifted from the homogeneous case. The shift is small because the interspecies boundary is located near the trap center where the trapping potential averaging effect is negligible. Yet, these studies often failed to identify a distinct transition point due to their limited sensitivity and relied primarily on observing morphological changes of the condensates.

Creating and investigating shell-shaped BECs based on immiscible dual-species BEC system represents a fundamentally different approach [24–26]. In spherically symmetric harmonic traps, the miscible-immiscible transition manifests as a hollowing transition where one species forms a shell surrounding the other—a topology drastically different from elongated geometries. This topological change leads to a dramatic shift in the interspecies boundary compared to previous studies. Furthermore, the shell location is highly sensitive to the harmonic confinement, the number of particles, and the interaction. Consequently, the transition exhibits much richer physics, displaying strong dependence on particle numbers and interaction strengths. The shell topology bestows BECs with distinctive features such as periodic boundaries, local curvature, and two surfaces, which are absent in BECs in standard bulk geometries. These features lead to a variety of unique properties, including the emergence of self-interference during free expansion [24,27,28], and the formation of vortex and antivortex pairs under fast rotation [29]. Two decades after the initial proposal, shell BECs have recently been successfully produced using several different methods, after overcoming the distortion of shell potentials caused by gravity [24,30]. The method based on immiscible double BECs allows the production of shell BECs without the need for a microgravity environment, making it more convenient for further exploration. For instance, the self-interference phenomenon was already studied in the first experiment based on this method [24].

---

[*] These authors contributed equally to this work.

[†] Present address: Institut für Experimentalphysik, Universität Innsbruck, Innsbruck, Austria.

[‡] Present address: Xi'an Institute of Applied Optics, Xi'an, China.

[§] Contact author: djwang@cuhk.edu.hk

In this work, we study the hollowing transition of the shell BEC using double-species ^{23}Na and ^{87}Rb BECs with tunable interspecies interactions. We employ the monopole mode of collective excitation as a sensitive probe of this transition [25,31,32], controlling the shell hollowness through a Feshbach resonance between the ^{23}Na and ^{87}Rb atoms. In the context of the dual-species BEC system, this study also provides direct access to collective excitation dynamics across the miscible-immiscible crossover, which has been theoretically studied previously [6,25], but has not been investigated experimentally. Here, in the out-of-phase monopole mode between the ^{23}Na and ^{87}Rb BECs with increasing repulsive interspecies interaction strengths, we observe a clear critical point as the ^{23}Na BEC transitions to a shell shape with a hollow center. We also find that this point depends sensitively on the atom number ratios between the two condensates. For typical experimental conditions, we find the hollowing transition occurs at an interspecies scattering length a_{12} of approximately $30a_0$, drastically different from the immiscible-miscible transition point of $a_{12} \approx 60a_0$ in elongated traps or free space.

II. EXPERIMENT

Our experiment starts with a dual-species BEC of ^{23}Na and ^{87}Rb atoms cotrapped in an optical dipole trap formed by crossing three orthogonally propagating 946-nm laser beams. To simplify the collective excitation spectrum, we create a nearly spherical harmonic potential by carefully adjusting the power ratios between the three laser beams. The measured oscillation frequencies of the trap along different axes are consistent with each other to within 5%. At the 946-nm "magic" wavelength [24,33], the two species experience the same trap oscillation frequency ω_0 and thus the same gravitational sag $-g/\omega_0^2$ in the vertical direction. This ensures the centers of mass of the two condensates nearly overlap.

We prepare both ^{23}Na and ^{87}Rb atoms in their lowest hyperfine Zeeman level $|F = 1, m_F = 1\rangle$. Away from Feshbach resonances, the interaction constants satisfy $g_{12} \geqslant \sqrt{g_{11}g_{22}}$, rendering the two condensates immiscible. Here, $g_{ij} = 2\pi\hbar^2 a_{ij}/\mu_{ij}$ where a_{ij} are the *s*-wave scattering lengths, $\mu_{ij} = m_i m_j/(m_i + m_j)$ are the reduced masses, and m_i are the atomic masses, respectively (with $i, j = 1$ for ^{23}Na and 2 for ^{87}Rb). Under these conditions, the ^{23}Na BEC will form a shell surrounding the ^{87}Rb BEC [24].

To control the hollowness of the ^{23}Na BEC, we use a magnetic Feshbach resonance at $B_0 = 347.65$ G to tune a_{12} following $a_{12} = a_{bg}[1 + \Delta/(B - B_0)]$. Here $a_{bg} = 76.3a_0$ is the background ^{23}Na - ^{87}Rb scattering length near B_0, and $\Delta = 4.26$ G is the width of the resonance [34]. By adjusting the magnetic field B from 351.91 to 370 G, we can modify a_{12} from $0a_0$ to $60a_0$ while keeping $a_{11} = 60.5a_0$ [35] and $a_{22} = 100.14a_0$ [36] constant. As shown in Fig. 1(a), numerical simulations using the coupled Gross-Pitaevskii equations (GPEs) suggest that within the range of a_{12}, intermediate states between a bulk and a shell sample of ^{23}Na BEC can be achieved.

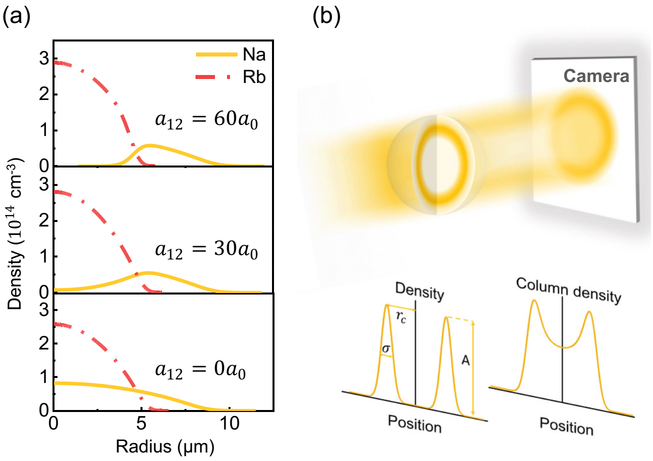

FIG. 1. Creating and probing a shell BEC in a ^{23}Na - ^{87}Rb double-species BEC system. (a) From bottom to top: calculated density distributions of the two condensates with increasing interspecies scattering length a_{12} illustrate the miscible-immiscible phase transition and the hollowing transition of the ^{23}Na shell. (b) During absorption imaging, a hollow shell appears as a double-peaked feature. The bottom subfigures depict the central intersections of the original shell (left) and its projection along the probing beam direction (right). The size of the shell can be extracted from the projected distribution using our fitting protocol.

III. IN-PHASE AND OUT-OF-PHASE MONOPOLE MODES

Analogous to classical coupled oscillators, the collective excitation of dual-species BECs also includes in-phase and out-of-phase modes. In general, the two modes are coupled [6,25], and probing them independently in experiments presents significant challenges. However, this issue can be mitigated by using the magic-wavelength spherical trap. Figures 2(a) and 2(b) show the numerically calculated spectra as a function of the interspecies scattering length for several of the lowest monopole modes using Bogoliubov–de Gennes equations (BdGEs), with the trapping light frequency set at the magic condition and slightly deviated from it, respectively. In

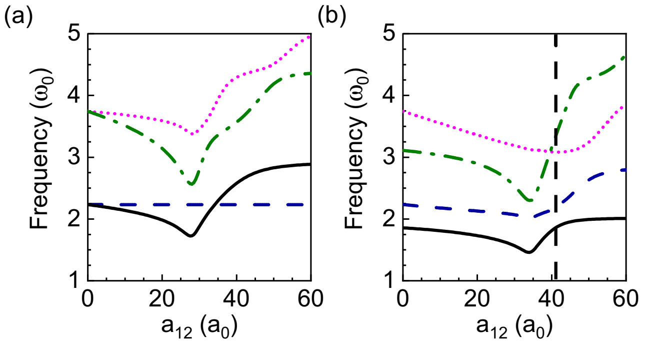

FIG. 2. Simplifying the double BECs excitation spectrum with magic-wavelength spherical potential. All plots are calculated using $N_1 = N_2 = 10^6$. (a) and (b) show the lowest four modes in magic-wavelength and non-magic-wavelength spherical traps, respectively. For the former, the trap oscillation frequencies are $2\pi \times 118.6$ Hz for both species, while for the latter, it is $2\pi \times 98.6$ Hz for ^{87}Rb. While in (a) the lowest in-phase (blue dashed curve) and out-of-phase modes (black solid curve) have no coupling, the same modes in (b) are coupled together as evidenced by the avoided crossing and the gap at the position marked by the vertical dashed line.

the magic-wavelength case, the two modes are fully decoupled and exhibit a real crossing, thus allowing them to be probed with minimal ambiguity. Conversely, in the latter case, the coupling leads to an avoided crossing with an energy gap, resulting in a switch between the in-phase and out-of-phase modes.

Intuitively, these very different behaviors can be understood as follows: when the trap frequencies for the two species differ, the excitation of the two species at small a_{12} exhibits a predominantly “single-species nature,” where one species is generally more significantly excited than the other. Such excitation is inherently a superposition of in-phase and out-of-phase characteristics, making it difficult to distinguish between the two modes. As a_{12} increases and the interspecies coupling becomes stronger, the modes transition to a “two-species nature,” where both species are substantially involved. This transition is characterized by a redistribution of the in-phase and out-of-phase contributions, resulting in coupled modes with mixed characteristics. In a magic-wavelength spherical trap with equal trap frequencies, the bare single-species excitation is degenerate even for $a_{12} = 0$. Importantly, the interspecies interaction resolves this degeneracy by forming collective eigenmodes that are purely in phase and purely out of phase. So, the two-species natures are originated from a_{12} and hence will not be altered by increasing a_{12}. As a result, the two modes are decoupled for all a_{12} in this special trap.

We note that the coupling appears even for small nonzero trap frequency difference $\Delta\omega$ and the gap moves to different a_{12} when $\Delta\omega$ is tuned. We define and calculate a quantity called the two-species collectivity, which equals 1 when both species contribute equally to the excitation and approaches zero when one species dominates. For $\Delta\omega = 0$ in the magic-wavelength trap, the collectivity remains high even for small a_{12}. However, it rapidly decreases for nonzero $\Delta\omega$, indicating that the excitation loses its two-species nature (see Appendix B 1). Thus, to clearly distinguish the in- and out-of-phase modes, especially at small a_{12}, the magic-wavelength spherical trap is essential. In addition, a spherical potential supports monopole modes without damping [37] and is generally easier to handle with analytical and computational methods. These advantages make the magic-wavelength spherical trap an ideal choice for detailed comparisons between our measurements and theoretical models.

We use two very different modulation methods to excite these two modes. In the first experiment, we excite and study the in-phase monopole mode by modulating the trapping potential. We first prepare the dual-species BEC at a target interspecies scattering length a_{12} by tuning the magnetic field. Subsequently, we modulate the power of the three trapping beams with the same phase and amplitude, which induces synchronized compression and expansion of the two condensates. The trap modulation amplitude and duration need to be set carefully to maximize the amplitude of the monopole oscillation while avoiding the excitation of other collective modes. Empirically, we determine that a modulation amplitude of 4% and a duration of approximately 15 modulation periods can induce large enough monopole oscillation amplitude without significantly coupling to other modes.

To excite the out-of-phase mode, we instead vary a_{12} by applying a sinusoidal modulation to the magnetic field while keeping the trapping potential constant. This modulation induces antiphased changes to the sizes of the two condensates. For instance, when a_{12} is increased, the ^{23}Na cloud is forced outward, causing it to expand, while the ^{87}Rb cloud is compressed inward, resulting in a size decrease. The dynamic interplay between the two condensates under this modulation scheme leads to the out-of-phase monopole oscillations of our interest.

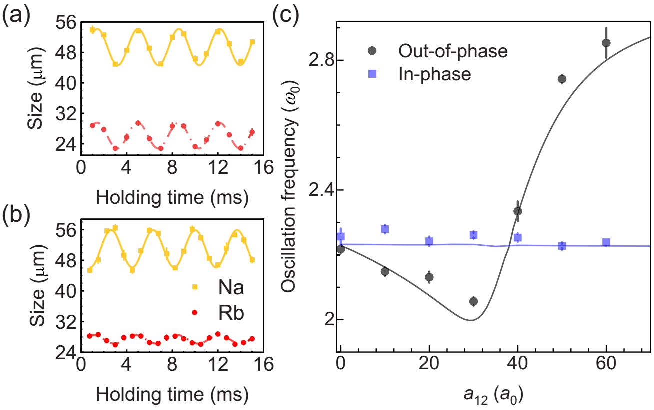

FIG. 3. (a) In-phase size oscillation for ^{87}Rb and ^{23}Na at $a_{12} = 30a_0$. For ^{87}Rb, data points represent the averaged horizontal and vertical sizes extracted from two-dimensional Gaussian fittings of the images, while for ^{23}Na, r_c obtained from the shell fitting procedure are used. (b) The out-of-phase size oscillation at $a_{12} = 30a_0$. (c) Frequency spectrum for the lowest in-phase and out-of-phase modes. The blue and black solid lines are the calculations from BdGEs for the lowest in-phase and out-of-phase monopole modes, respectively. For this set of measurements, the ^{23}Na atom number is $1.0(2) \times 10^5$ and the ^{87}Rb atom number is $7.0(5) \times 10^4$. All oscillation frequencies ω are normalized to the trap frequency ω_0. The error bars of ω are from the sinusoidal fitting.

Similar to that for the in-phase mode, we empirically choose the amplitude and duration of the a_{12} modulation to obtain the maximum possible signal without significant excitation of other collective modes. For small a_{12}, we use a moderate modulation amplitude of $2a_0$ which is enough to cause significant sample size variations. However, when a_{12} becomes large enough to cause phase separation, we increase the modulation amplitude to $5a_0$ to compensate for the reduced overlap and effectively excite the desired oscillation.

After modulation, we allow the two condensates to evolve in the trap for varying durations. Finally, we release them from the trap and image the resulting clouds using a two-species high-magnetic-field absorption imaging method after 15 ms of free expansion [38]. As illustrated in Fig. 1(b), to obtain the size of the ^{23}Na shell, we model it with a three-dimensional spherical Gaussian shell function $n_1 \times \exp[-(r - r_c)^2/\sigma^2]$. We fit the absorption images using the Abel transformation of this Gaussian shell function to extract the shell center r_c, shell thickness σ, and peak density n_1. We use r_c to represent the size of the ^{23}Na shell. For the ^{87}Rb BEC size and ^{23}Na bulk sample when a_{12} is small, we use the average of the horizontal and vertical rms widths obtained from two-dimensional Gaussian fits.

Figures 3(a) and 3(b) are exemplary resulting monopole oscillations of two miscible condensates with $a_{12} = 30a_0$ excited by modulating the trapping potential and the interspecies interaction strength, respectively. For the former case, the measured phase slip between the ^{23}Na and ^{87}Rb size oscillations is less than 0.1π, which is consistent with in-phase oscillation; for the latter in Fig. 3(b), this is about 1.1π, i.e., the two condensates oscillate out of phase with each other. As expected for a spherical potential [37], the damping is minimal during the observation period. The slight phase slip and damping are attributed to residual mixing between the two modes, most possibly due to the imperfect spherical symmetry and unavoidable anharmonicity of the optical potential.

IV. THE HOLLOWING TRANSITION

To investigate the hollowing transition, we examine the monopole modes for a_{12} from 0 to around $60a_0$. As will be discussed later, the oscillation frequency ω of the out-of-phase mode also depends on the atom numbers. The atom number fluctuations in our system are large enough to generate observable effects. To mitigate this problem, we used only postselected data points with atom number fluctuations within 20% for this measurement.

The blue points in Fig. 3(c) show the measured oscillation frequency ω of the in-phase mode, which barely changes with a_{12}. This is reminiscent of the in-phase normal mode of two classical coupled oscillators with the same natural frequencies, where the coupled oscillation frequency is the same as that of the individual uncoupled oscillators and is not affected by the coupling. Here, the measured ω is $\sqrt{5}\omega_0$, exactly the same as that of the monopole mode for individual BECs in the Thomas-Fermi (TF) regime [39]. This agrees with our theoretical derivation (see Appendix B 2) which shows that the two-species BEC can be effectively treated as a single one in this mode. Obviously, this mode is not sensitive to the hollowing transition.

The behavior of the out-of-phase mode is drastically different, as shown by the black points in Fig. 3(c). For two noninteracting condensates at $a_{12} = 0a_0$, the oscillation frequency ω is also $\sqrt{5}\omega_0$, the same as that of the in-phase mode. As a_{12} increases, ω first decreases to a minimum of approximately $2\omega_0$ at $30a_0$. Afterwards, it starts to increase and eventually levels off for $a_{12} \geqslant 60a_0$ when the Na shell is fully formed. This nonmonotonic dependence on a_{12} thus makes this mode a sensitive probe of the hollowing transition.

While this behavior agrees fully with our numerical solution based on BdGEs [black solid curve in Fig. 3(c)], an intuitive understanding can be gained from the fact that the out-of-phase mode involves density oscillations transverse to the condensate boundaries, where the relative motion between the two species makes ω sensitive to the overlap, and thus a_{12} [31]. In addition, this mode predominantly excites the ^{23}Na shell, while the bulk ^{87}Rb BEC is driven to respond with an opposite-sign motion to minimize the interaction energy. This is evident from the π-phase difference between the two species and the larger oscillation amplitude of ^{23}Na, as shown in Fig. 3(b). This suggests that we can gain insight by studying the thin-shell limit with $N_1 \ll N_2$ [27], where ^{23}Na dominates the mode dynamics and ^{87}Rb excitation, being the response, becomes less important. Here N_1 and N_2 are the numbers of ^{23}Na and ^{87}Rb atoms, respectively. This allows an analysis with the simplified BdGEs, which can quantitatively reproduce the frequency spectrum of the full BdGEs (see Appendix B 3).

Under such a limit, the ^{87}Rb BEC merely acts as a background, contributing to an effective potential $V_{\text{eff}}(r) = \frac{1}{2}m_1\omega_0^2r^2 + g_{12}n_2(r)$ for ^{23}Na. Here $n_2(r)$ is the ground-state density distribution of ^{87}Rb. For the small a_{12} region before the shell starts to form, since the two condensates are miscible, under the TF approximation,

$$V_{\text{eff}}(r) = \tfrac{1}{2}m_1\tilde{\omega}_0^2r^2 + C, \tag{1}$$

where

$$\tilde{\omega}_0 = \omega_0\left(1 - \frac{g_{12}m_2}{2g_{22}m_1}\right) \tag{2}$$

is a weakened trap frequency and C is a constant shift. The simplified two-species BdGEs reduce the system to the single-species case with a collective oscillation frequency $\omega = \sqrt{5}\tilde{\omega}_0$ (see Appendix B 3). For cases with more balanced numbers $N_1 \sim N_2$, we can use a hydrodynamic analysis instead (see Appendix B 2), which gives $\omega = \sqrt{5}\omega_0(1 - \frac{g_{12}m_1}{g_{11}m_2})$. For both scenarios, the reduction of ω with increasing a_{12} before the hollowing transition is well accounted for by these analyses.

The posthollowing increase in ω can also be understood with the effective potential $V_{\text{eff}}(r)$. At large a_{12}, when the inner surface of the shell is formed, the shell experiences a skewed "V"-shape $V_{\text{eff}}(r)$, with its minimum at the equilibrium position r_c. Approximating $V_{\text{eff}}(r)$ as harmonic, its steepness qualitatively determines ω of the shell BEC. As a_{12} increases, the potential becomes steeper and ω increases. However, at very large a_{12}, $V_{\text{eff}}(r)$ transforms into a hard wall potential plus a linear term. Further strengthening of the wall no longer affects the dynamics, leading to the observed plateau in the frequency spectrum.

From a physical standpoint, at small a_{12}, the ^{23}Na BEC oscillates like an accordion [27], with only its width changing. In this regime, density modulations are localized in the center, where both condensates experience a weakened trap. This leads to reduced densities and lower stiffness, resulting in lower ω that does not depend on N_1. As a_{12} increases, the ^{87}Rb condensate becomes a rigid core for the ^{23}Na shell, creating an inner boundary. This boundary restricts the motion of the width and therefore restores the stiffness. Furthermore, it liberates and shifts the dominant motion degree of freedom to r_c, where the ^{23}Na BEC oscillates like a balloon [27] with higher ω. Thus, the emergence of the inner boundary changes the trend, creating a minimum in the out-of-phase mode frequency spectrum. This minimum is a hallmark of the transition point.

V. THE EFFECT OF ATOM NUMBERS

Next, we investigate the dependence of the hollowing transition on the number of atoms. To this end, we measure the out-of-phase oscillation frequency ω as a function of a_{12},

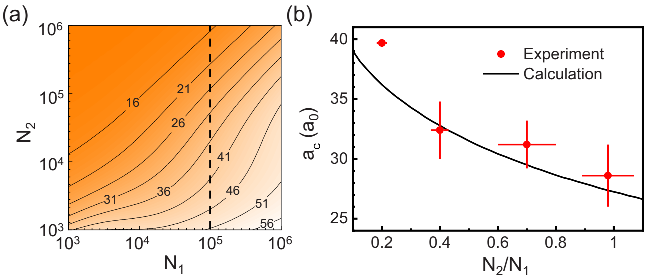

FIG. 4. The effect of number ratio on the hollowing transition point. (a) The numerically calculated a_c (in units of a_0) for the hollowing transition with different combinations of ^{23}Na and ^{87}Rb atom numbers. (b) Experimentally measured a_c for several number ratios N_2/N_1 between ^{87}Rb and ^{23}Na. The ^{23}Na number is fixed at approximately 1×10^5, thus the theoretical curve corresponds to the black vertical dashed line in (a). The error bars of N_2/N_1 are from statistics of number fluctuations, while those of the a_c are from the fitting.

similar to that shown in Fig. 3(c), for various ratios of ^{87}Rb to ^{23}Na atom numbers N_2/N_1. Figure 4(a) shows the calculated general behavior of the critical interspecies scattering length a_c for all combinations of atom numbers ranging from 10^3 to 10^6, illustrating that the hollowing transition point is highly sensitive to the atom number ratios. In the experiment, we fix N_1 at approximately 10^5 and vary N_2 from 2×10^4 to 10^5 for each set of measurements. This allows us to probe the out-of-phase monopole mode for N_2/N_1 ranging from 0.2 to 1. We then empirically fit each spectrum with a bi-Gaussian function, sharing the same center positions but having different widths, to extract the a_c at the minimum of ω, which corresponds to the onset of the hollowing transition.

The measured a_c as a function of number ratio N_2/N_1 is summarized in Fig. 4(b). The observed decrease in the a_c with increasing N_2/N_1 indicates that the ^{23}Na BEC forms a shell structure at progressively smaller a_{12} values as the ^{87}Rb number increases. This behavior is attributed to the contribution of the ^{87}Rb BEC to $V_{\text{eff}}(r)$. As the repulsion experienced by ^{23}Na from ^{87}Rb is $g_{12}n_2 \sim g_{12}N_2^{2/5}$, increasing N_2 hardens the ^{87}Rb core and lowers the interaction strength needed for ^{23}Na to become hollow.

However, it is worth noting that when the number of atoms in either species becomes very low, the quantum pressure term starts to play a significant role in the hollowing transition. This explains why the a_c saturates in the upper-left and lower-right regions of Fig. 4(a). The larger deviation of the data point at $N_2/N_1 = 0.2$ from the theoretical curve can be attributed to the less pronounced frequency minimum, which reduces the reliability of the fitting procedure used to extract it (see Appendix A 3).

VI. CONCLUSION

In this work, we demonstrate a powerful approach to probe the quantum topology change in shell-shaped BECs through collective excitations. Through precise control of the shell-BEC hollowing transition and comprehensive measurements of its collective modes, we establish definitive experimental evidence of the topological changes between filled and hollow condensates. Our measurements unambiguously identify two distinct monopole modes with dramatically different behaviors: a robust in-phase mode with constant frequency, and a highly sensitive out-of-phase mode that exhibits pronounced nonmonotonic frequency response marking the topological transition point. Exploiting this hallmark of the transition, we reveal the critical dependence of the hollowing transition on the number ratio of the two species, showcasing a key mechanism that governs shell formation. Our results establish collective excitations as a precise and effective tool for investigating quantum topology transitions in ultracold gases. The significant deviation of the hollowing transition point from conventional miscible-immiscible transitions in elongated traps conclusively demonstrates the uniquely rich physics emerging from the exotic shell topology, opening new avenues for exploring quantum many-body phenomena in curved spaces.

ACKNOWLEDGMENTS

This work was supported by the Hong Kong RGC General Research Fund (Grants No. 14301620 and No. 14302722) and the Collaborative Research Fund C4050-23G, Guangdong Provincial Quantum Science Strategic Initiative (Grants No. GDZX2303002 and No. GDZX2404004), and Space Application System of China Manned Space Program.

DATA AVAILABILITY

The data that support the findings of this article are not publicly available. The data are available from the authors upon reasonable request.

APPENDIX A: EXPERIMENTAL METHODS AND DATA ANALYSIS

1. The spherical magic-wavelength trap

The procedure for preparing the shell BEC sample is similar to our previous work [15,24]. Initially, we evaporate the double BECs in a crossed 1070-nm optical dipole trap and subsequently load them into a 946-nm optical dipole trap at low magnetic field. We then ramp up the magnetic field to reach the desired value. To realize a spherical potential, we then introduce an additional 946-nm laser beam in the vertical direction [Fig. 5(a)]. By fine tuning the power of this vertical beam, we finally obtain equal trap frequencies along all directions.

The trap frequency of the spherical trap is determined by observing the sloshing motion of the BEC sample from two different directions [37,40]. We begin by applying a small magnetic gradient pulse for a short duration to displace the sample from its equilibrium position and then turn off the gradient. After a variable evolution time, we release the BEC from the trap and image it after 15 ms of time of flight. The axes of the trapping potential are defined in a rotated frame (x', y', z') relative to the reference frame (x, y, z) set by the imaging axis. In the frame of the trapping potential, the

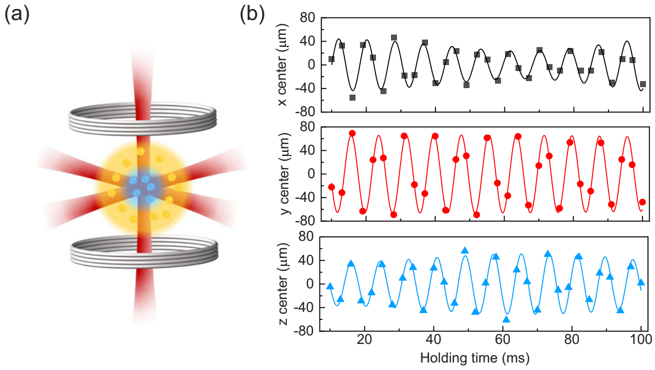

FIG. 5. (a) Creating a magic-wavelength spherical optical potential by crossing three laser beams. The asphericity is fined tuned by adjusting the relatively powers of the beams. (b) Characterizing the spherical trap via sloshing motions simultaneously in all three directions. For this set of data, the trap frequencies obtained from the global fitting are $(\omega_{x'}, \omega_{y'}, \omega_{z'}) = 2\pi \times [122.3(3), 128.6(7), 124.8(1)]$ Hz (see text for details).

position of the atomic cloud is given by

$$\mathbf{r}' = \begin{bmatrix} A_{x'} \sin(\omega_{x'}t + \phi_{x'}) \\ A_{y'} \sin(\omega_{y'}t + \phi_{y'}) \\ A_{z'} \sin(\omega_{z'}t + \phi_{z'}) \end{bmatrix} \tag{A1}$$

where $A_{i'}$, $\omega_{i'}$, and $\phi_{i'}$ $(i' = x', y', z')$ are the amplitude, angular frequency, and phase of the oscillation along the eigenaxes of the potential. In the imaging axis frame, the position of the atomic cloud is given by

$$\mathbf{r} = \mathbf{R}_z(\theta_z)\mathbf{R}_y(\theta_y)\mathbf{R}_x(\theta_x)\mathbf{r}' \tag{A2}$$

where $R_i(\theta_i)$ is the rotation matrix which rotates the coordinate system around axis i'.

We perform a global fit of Eq. (A2) to the atomic cloud position obtained from both horizontal and vertical imaging. An example of the observed oscillation is shown in Fig. 5(b). The geometric mean of the trap frequencies $\omega_0 = (\omega_{x'}\omega_{y'}\omega_{z'})^{1/3}$ is used for data analysis.

Since the spherical potential is critical for decoupling the in-phase and out-of-phase modes, and to minimize the effect of damping, we typically collect data using a spherical potential with a residual asphericity less than 5%. The asphericity is defined as $(\omega_{\max} - \omega_{\min})/\omega_0$, where $\omega_{\max}$ and $\omega_{\min}$ are the maximum and minimum of the three trap frequencies, respectively.

2. Shell fitting

Instead of using the lightsheet imaging method as in our previous work [24], we adopt a shell fitting method to better extract information from the shell [41]. An example of the fitting is shown in Fig. 6.

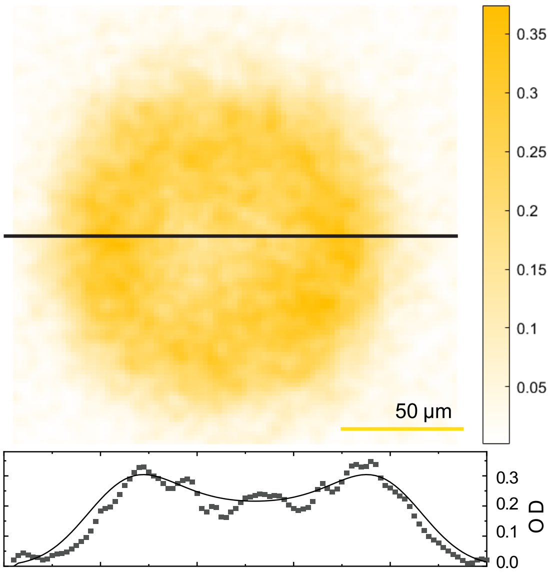

FIG. 6. Example of the fitting results. The bottom panel shows the fitting results for the data points indicated by the black line in the upper image.

3. Transition point

To extract the critical interspecies scattering length a_c for the hollowing transition, we fit the data empirically using a bi-Gaussian function with the same center position but different widths:

$$f(x) = \begin{cases} A\exp\left(-\dfrac{(a_{12}-a_c)^2}{2\sigma_L^2}\right) + B, & a_{12} < a_c, \\ A\exp\left(-\dfrac{(a_{12}-a_c)^2}{2\sigma_R^2}\right) + B, & a_{12} \geqslant a_c. \end{cases} \tag{A3}$$

Here, A is the amplitude, B is the offset, and σ_L and σ_R are the widths on the left and right sides of a_c, respectively.

An example is shown in Fig. 7, where for $N_2/N_1 = 0.4$ the critical interspecies scattering length of the hollowing transition is determined to be $a_c = 32(2)a_0$ from the fitting.

The uncertainty of the critical interspecies scattering length, a_{12}, is derived from the fitting error. This fitting procedure employs a weighted least-squares approach, where each measured frequency data point contributes to the fit according to a weight inversely proportional to its variance.

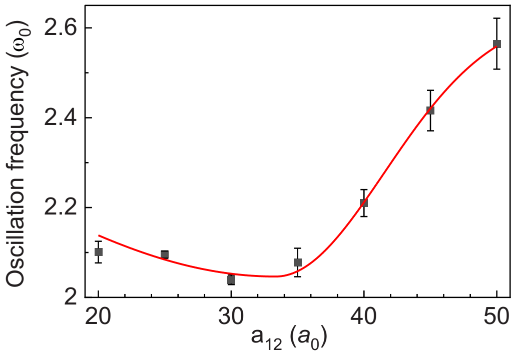

FIG. 7. Bi-Gaussian fit of the out-of-phase mode spectrum for extracting the transition point of the hollowing transition. The black squares are the measured oscillation frequencies at different a_{12}, while the curve is from the fitting to the bi-Gaussian in Eq. (A3).

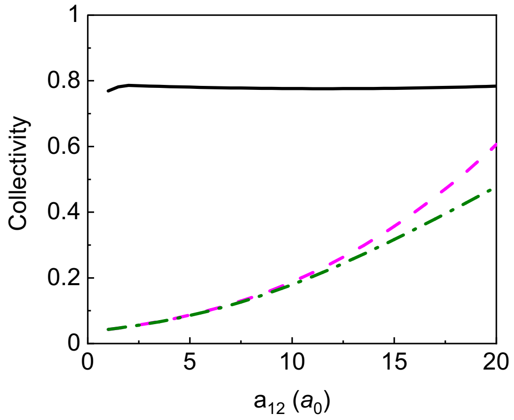

FIG. 8. Collectivity between species excitations, showing the average of in-phase and out-of-phase modes. Solid line, trap frequencies $\omega_1 = \omega_2 = 2\pi \times 118.6\,\mathrm{Hz}$; dashed, $\omega_1 = 2\pi \times 108.6\,\mathrm{Hz}$, $\omega_2 = 2\pi \times 118.6\,\mathrm{Hz}$; dash-dotted, $\omega_1 = 2\pi \times 118.6\,\mathrm{Hz}$, $\omega_2 = 2\pi \times 108.6\,\mathrm{Hz}$. Data at $a_{12} = 0a_0$ are omitted. For large a_{12}, the collectivity is always high due to the interspecies interaction.

It is important to note that the fitting routine evaluates only how well the weighted data points agree with the chosen fitting function, and the reported error on a_{12} reflects the formal error of this fit alone. It does not account for the propagation of uncertainties from the original data points.

Specifically, for the case of $N_2/N_1 = 0.2$, the frequency dip at the hollowing transition is relatively shallow. Under such circumstances, minor fluctuations in the measured frequencies near the transition region can notably affect the fitting results. Given that the fitting algorithm optimizes overall data agreement rather than explicitly emphasizing sensitivity near critical transitions—and considering the limited number of available data points—these fluctuations may introduce biases into the determined a_{12} values that are not fully captured by the reported uncertainty. This scenario explains why the uncertainty appears smaller than expected in the point of $N_2/N_1 = 0.2$ in Fig. 4.

APPENDIX B: THEORETICAL ANALYSIS

1. Collectivity

We define collectivity between two species as

$$\text{Collectivity} = 1 - \tanh\left(2 \times \frac{|\Delta N_1 - \Delta N_2|}{\Delta N_1 + \Delta N_2}\right), \tag{B1}$$

where $\Delta N_i = \int |\delta n_i(r)| d^3 r$ is the number of particles involved in the excitation with density modulation $\delta n_i(r)$. The factor 2 serves as a scale where the case $\Delta N_i = 3\Delta N_j$ defines large particle imbalances, and the hyperbolic tangent enhances the sensitivity to imbalances.

With this definition, the collectivity is 1 when both species contribute equally to the excitation and approaches zero when one species dominates. As shown in Fig. 8, this is particularly relevant for small a_{12} when the interaction is weak. At matched trapping frequencies, the collectivity remains high even in this regime. However, when the trap frequencies are different for the two species, the collectivity rapidly decreases, indicating that the excitations lose their two-species nature. In this sense, the magic-wavelength spherical trap is necessary in order to probe the hollowing transition. For larger a_{12}, collectivity is always high as interaction already couples two species.

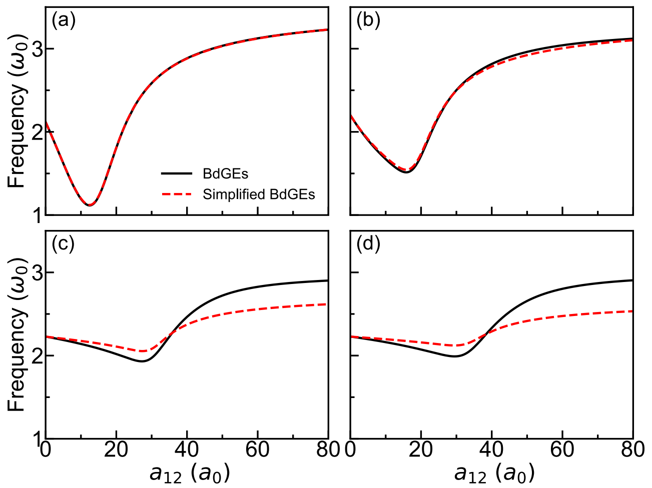

FIG. 9. Comparison of the lowest out-of-phase monopole mode spectrum with full BdGEs (solid curves) and the simplified BdGEs (dashed curves) for several different atom numbers. (a) $N_1 = 10^3$ and $N_2 = 10^5$. (b) $N_1 = 10^4$ and $N_2 = 10^5$. (c) $N_1 = 10^5$ and $N_2 = 10^5$. (d) $N_1 = 10^5$ and $N_2 = 7 \times 10^4$.

2. Hydrodynamics equation method for balanced $N_1 \sim N_2$

a. Single-species hydrodynamics equations

From the TF approximation, the ground-state density distribution for the single-species case in an isotropic harmonic trap is [42]

$$n_i(r) = \frac{1}{2}\frac{m_i}{g_{ii}}\omega_0^2\left(R_i^2 - r^2\right). \tag{B2}$$

R_i is determined from the conservation of the number of particles. To consider the collective excitation, a perturbative term is added such that the general density distribution is written as $n_i(\mathbf{r}, t) \mapsto n_i(r) + \delta n_i(\mathbf{r})e^{-\mathrm{i}\omega t}$; this leads to an eigenvalue problem [42]:

$$-m_i\omega^2\delta n_i(\mathbf{r}) = \nabla \cdot [g_{ii}n_i(r)\nabla\delta n_i(\mathbf{r})]. \tag{B3}$$

We are interested in the breathing mode with $\omega = \sqrt{5}\omega_0$ and [42]

$$\delta n_i(\mathbf{r}) = C_i\left(1 - \frac{5}{3}\frac{r^2}{R_i^2}\right), \tag{B4}$$

where C_i is an undetermined constant.

b. Two-species hydrodynamics equations

In the two species case, the ground-state density profile can be obtained from the TF approximation as

$$\begin{pmatrix} g_{11} & g_{12} \\ g_{12} & g_{22} \end{pmatrix}\begin{pmatrix} n_1 \\ n_2 \end{pmatrix} = \begin{pmatrix} \mu_1 \\ \mu_2 \end{pmatrix} + \frac{1}{2}\omega_0^2 r^2 \begin{pmatrix} m_1 \\ m_2 \end{pmatrix}, \tag{B5}$$

where n_i is obtained by inverting the interaction matrix on the left. To describe the excitation, the hydrodynamics equations that describe the BECs in terms of the densities and the velocity field $\mathbf{v}_i(\mathbf{r},t)$ are

$$m_i\frac{\partial \mathbf{v}_i}{\partial t}=-\nabla\left(\frac{1}{2}m_i\left(v_i^2+\omega_0^2r^2\right)+g_{ii}n_i+g_{12}n_j\right),$$
$$\frac{\partial n_i}{\partial t}+\nabla\cdot(n_i\mathbf{v}_i)=0. \tag{B6}$$

To analyze the excitations, we follow the single-species case and substitute $n_i(\mathbf{r},t)\mapsto n_i(r)+\delta n_i(\mathbf{r},t)$ and $\mathbf{v}_i(\mathbf{r},t)\mapsto 0+\delta\mathbf{v}_i(\mathbf{r},t)$ into Eq. (B6). Up to first order in δn_i and $\delta\mathbf{v}_i$, the two equations in Eq. (B6) are combined into a single one, and substituting $\delta n_i(\mathbf{r},t)=\delta n_i(\mathbf{r})e^{\mathbf{i}\omega t}$ yields

$$-m_i\omega^2\delta n_i=\nabla\cdot[n_i\nabla(g_{ii}\delta n_i+g_{12}\delta n_j)], \tag{B7}$$

where the time-dependent phase is canceled out and this equation determines the frequency spectrum.

c. Perturbative analysis

This section obtains a perturbative description for the breathing mode when $g_{12}\approx 0$ and ^{23}Na encloses ^{87}Rb ($R_1\gtrsim R_2$). We focus on ^{87}Rb because only the overlapping region needed to be considered.

We analyze Eq. (B7) by keeping up to first order in g_{12}, with quantities being expanded as

$$n_i(r)=n_i^{(0)}(r)+g_{12}\Delta n_i(r),$$
$$\mu_i=\mu_i^{(0)}+g_{12}\Delta\mu_i,$$
$$\delta n_1(r,t)=s\left[\delta n_1^{(0)}(r)+g_{12}h_1(r)\right]e^{-\mathbf{i}(\sqrt{5}\omega_0+g_{12}\omega')t},$$
$$\delta n_2(r,t)=\left[\delta n_2^{(0)}(r)+g_{12}h_2(r)\right]e^{-\mathbf{i}(\sqrt{5}\omega_0+g_{12}\omega')t}, \tag{B8}$$

where the superscript "0" is to denote the case when $g_{12}=0$, say, $n_i^{(0)}$ is the ground-state distribution in the absence of interspecies interaction. The first-order correction in frequency is $g_{12}\omega'$, and $s=+1$ for the in-phase mode and $s=-1$ for the out-of-phase mode. To find ω' and $h_i(r)$, we obtain the $\Delta n_i(r)$ through Eq. (B5) and substitute directly the expansion in Eq. (B8) into Eq. (B7), leading to a complicated equation. We can simplify the equation by rewriting $n_1^{(0)}\nabla\delta n_2^{(0)}$ and $n_2^{(0)}\nabla\delta n_1^{(0)}$ with the explicit expressions in Eqs. (B2) and (B4), and further postulating that the constants C_i in Eq. (B4) are related by

$$\frac{C_1}{C_2}=\frac{\frac{1}{2}\frac{m_1}{g_{11}}\omega_0^2R_1^2}{\frac{1}{2}\frac{m_2}{g_{22}}\omega_0^2R_2^2}=\frac{g_{22}m_1R_1^2}{g_{11}m_2R_2^2}. \tag{B9}$$

This means that the peak excitation amplitude is proportional to the peak density of the ground-state distribution. Eventually, we cancel some terms using Eq. (B3), and obtain the eigenvalue equations

$$-\sqrt{5}\omega_0m_2\delta n_2^{(0)}\left(2\omega'+(1-s)\frac{m_1}{g_{11}m_2}\sqrt{5}\omega_0\right)=B+5m_2\omega_0^2h_2+\nabla\cdot\left[g_{22}n_2^{(0)}\nabla h_2\right]=5m_2\omega_0^2\tilde{h}_2+\nabla\cdot\left[g_{22}n_2^{(0)}\nabla\tilde{h}_2\right], \tag{B10}$$

where B is a constant and $\tilde{h}_2\equiv h_2+B/(5\omega_0^2m_2)$. There is a simple solution to this equation when $\tilde{h}_2$ has the same form as Eq. (B4), such that $\nabla\cdot[g_{22}n_2^{(0)}\nabla\tilde{h}_2]=-5m_2\omega_0^2\tilde{h}_2$ and the term in parentheses in Eq. (B10) is equal to zero, giving rise to

$$\omega'=\begin{cases}0, & \text{in phase}\\ -\sqrt{5}\omega_0\frac{m_1}{g_{11}m_2}, & \text{out of phase.}\end{cases} \tag{B11}$$

The in-phase mode frequency is again a constant $\sqrt{5}\omega_0$. The out-of-phase excitation frequency is

$$\omega=\sqrt{5}\omega_0+g_{12}\omega'=\sqrt{5}\omega_0\left(1-\frac{g_{12}m_1}{g_{11}m_2}\right). \tag{B12}$$

Such a solution of h_2 means that the interspecies interaction solely modulates the amplitude $\delta n_2^{(0)}$ and introduces a constant shift, hinting that ^{23}Na acts as a background for ^{87}Rb. To obtain h_1, one can flip the indices in Eq. (B10) and substitute the determined ω', then solve the resultant equation. For the in-phase mode, h_1 has a similar form as Eq. (B4) up to a constant. Hence both species retain the single-species nature. For the out-of-phase mode, $h_1$does not have analytical form and is beyond our interest.

3. Simplified BdGEs in the thin-shell limit for $N_1\ll N_2$

We focus on the case where ^{87}Rb encloses ^{23}Na ($R_2>R_1$). For weak g_{12}, inverting the interaction matrix in Eq. (B5) and expanding g_{12} to first order yields the ^{23}Na's density distribution:

$$n_1(r)=\frac{1}{2}\frac{m_1}{g_{11}}\tilde{\omega}_0^2\left(\tilde{R}_1^2-r^2\right), \tag{B13}$$

where $\tilde{\omega}_0=\omega_0[1-g_{12}m_2/(2g_{22}m_1)]$ is the effective trapping frequency and $\tilde{R}_1>R_1$ is the TF radius under small g_{12}. The explicit form of $\tilde{R}_1$ can be found from the conservation of the number of particles, but it is not needed here. The single-species BdGEs when $g_{12}=0$ and under TF approximation are [42]

$$\left(-\frac{\hbar^2}{2m_1}\nabla^2+\frac{1}{2}m_1\omega_0^2\left(R_1^2-r^2\right)\right)u(r)+\left(\frac{1}{2}m_1\omega_0^2\left(R_1^2-r^2\right)\right)v(r)=\hbar\omega u(r),$$
$$\left(-\frac{\hbar^2}{2m_1}\nabla^2+\frac{1}{2}m_1\omega_0^2\left(R_1^2-r^2\right)\right)v(r)+\left(\frac{1}{2}m_1\omega_0^2\left(R_1^2-r^2\right)\right)u(r)=-\hbar\omega v(r), \tag{B14}$$

where $u(r)$ and $v(r)$ relate to the wave function as $\psi(r,t) = [\psi^{(0)}(r) + u(r)e^{-i\omega t} + v^*(r)e^{i\omega t}]e^{-i\mu t}$. $\psi^{(0)}(r)$ is the ground-state wave function. Note that $\mu_1 - \frac{1}{2}m_1\omega_0^2 r^2 = g_{11}n_1^{(0)}$.

The two-species simplified BdGEs are obtained by neglecting the excitations of ^{87}Rb. Denoting $\psi_1(r,t) = [\psi_1^{(0)}(r) + u(r)e^{-i\omega t} + v^*(r)e^{i\omega t}]e^{-i\mu_1 t}$, the simplified BdGEs are

$$\left(-\frac{\hbar^2}{2m_1}\nabla^2 + \frac{1}{2}m_1\omega_0^2 r^2 - \mu_1 + 2g_{11}n_1 + g_{12}n_2\right)u(r) + g_{11}n_1 v(r) = \hbar\omega u(r),$$

$$\left(-\frac{\hbar^2}{2m_1}\nabla^2 + \frac{1}{2}m_1\omega_0^2 r^2 - \mu_1 + 2g_{11}n_1 + g_{12}n_2\right)v(r) + g_{11}n_1 u(r) = -\hbar\omega v(r). \tag{B15}$$

In Fig. 9, we show the predicted out-of-phase spectra from numerically solving the full BdGEs and Eq. (B15) for different N_1 and N_2 as a comparison. We see that the simplified BdGEs provide excellent descriptions for small N_1. In TF approximation, since $\mu_1 = \frac{1}{2}m_1\omega_0^2 r^2 + g_{11}n_1 + g_{12}n_2$ in Eq. (B5), we find the terms inside the brackets in Eq. (B15) can be simplified as

$$\tfrac{1}{2}m_1\omega_0^2 r^2 - \mu_1 + 2g_{11}n_1 + g_{12}n_2 = g_{11}n_1 = \tfrac{1}{2}m_1\tilde{\omega}_0^2\big(\tilde{R}_1^2 - r^2\big). \tag{B16}$$

Therefore Eq. (B15) reduces to the form of Eq. (B14) with effective trap frequency $\tilde{\omega}_0$. If ^{23}Na is enclosed by ^{87}Rb ($R_2 > R_1$), the TF analysis for Eq. (B15) is valid for the whole distribution, where we obtain

$$\omega = \sqrt{5}\tilde{\omega}_0 = \sqrt{5}\omega_0\left(1 - \frac{g_{12}m_2}{2g_{22}m_1}\right). \tag{B17}$$

On the other hand, if ^{23}Na encloses ^{87}Rb ($R_1 > R_2$), we have to consider the ^{23}Na density in the nonoverlapping region. Equation (B16) is still true, but we have to consider the ^{87}Rb's excitation with effective frequency $\omega_0(1 - \frac{g_{12}m_1}{2g_{11}m_2})$ higher than ^{23}Na's and the nonoverlapping region with the original frequencies ω_0. Hence Eq. (B17) serves as a lower bound. Regardless of the cases, ω is lower than the single-species value $\sqrt{5}\omega_0$.

4. Variational method

a. Before hollowing transition

The Lagrangian for double-species BECs is [42]

$$\mathcal{L} = \int \left\{ \sum_i \left[\frac{\mathrm{i}\hbar}{2}\left(\psi_i^*\frac{\partial\psi_i}{\partial t} - \psi_i\frac{\partial\psi_i^*}{\partial t}\right) - \frac{\hbar^2}{2m_i}|\nabla\psi_i|^2 - V_i|\psi_i|^2 - \frac{g_{ii}}{2}|\psi_i|^4 \right] - g_{12}|\psi_1|^2|\psi_2|^2 \right\} d^3r. \tag{B18}$$

By assuming different forms of *Ansätze*, we describe the dual-species BECs in different regimes. For weak g_{12}, the oscillations of two species resemble that in the single-species case where the width of the condensate is oscillating [42], hence the *Ansätze* are set to be

$$\psi_1(r,t) = \frac{\sqrt{N_1}}{\sigma_1(t)^{3/2}} f_1\left(\frac{r}{\sigma_1(t)}\right) e^{\mathrm{i}\beta_1(t)m_1 r^2/(2\hbar)},$$

$$\psi_2(r,t) = \frac{\sqrt{N_2}}{\sigma_2(t)^{3/2}} f_2\left(\frac{r}{\sigma_2(t)}\right) e^{\mathrm{i}\beta_2(t)m_2 r^2/(2\hbar)}, \tag{B19}$$

where $\sigma_1(t)$, $\sigma_2(t)$, $\beta_1(t)$, and $\beta_2(t)$ are the variational parameters, and the functions $f_1(x)$ and $f_2(x)$ do not need to be known explicitly. r is the radial distance from the harmonic trap center. The length $\sigma_i(t)$ is the width of the distribution, and it is equal to a stationary value $\sigma_i^{(0)}$ in the ground state. The ground-state density profile defines $\sigma_i^{(0)}$ once the function $f_i(x)$ is chosen explicitly. Equivalently, Eq. (B19) represents the ground-state distribution when $\sigma_i(t) = \sigma_i^{(0)}$ [and $\beta_i(t) = 0$]. During the excitation, $\sigma_i(t)$ oscillates periodically around the equilibrium value with a small amplitude deviation $\tilde{\sigma}_i(t) \equiv \sigma_i(t) - \sigma_i^{(0)}$. The form of the phase $\beta_i(t)m_i r^2/(2\hbar)$ represents a velocity field $\beta_i(t)r\hat{r}$, where $\hat{r}$ is the radial unit vector. This choice of the phase characterizes the species's motion to be its width $\sigma_i(t)$. In the following, σ_i and $\sigma_i(t)$ are used synonymously, and similarly for other parameters. Putting the *Ansätze* into the Lagrangian Eq. (B18), we obtain

$$\mathcal{L} = -\big[\tfrac{1}{2}m_1N_1\sigma_1^2 c_{\mathrm{tr},1}\big(\dot{\beta}_1 + \beta_1^2\big) - U_1(\sigma_1)\big] - \big[\tfrac{1}{2}m_2N_2\sigma_2^2 c_{\mathrm{tr},2}\big(\dot{\beta}_2 + \beta_2^2\big) + U_2(\sigma_2)\big] - U_{12}, \tag{B20}$$

where

$$U_i(\sigma_i) = \frac{c_{\mathrm{ZP},i}}{\sigma_i^2} + \frac{1}{2} m_i N_i \omega_0^2 \sigma_i^2 c_{\mathrm{tr},i} + \frac{c_{\mathrm{int},i}}{\sigma_i^3} \Rightarrow E_{\mathrm{zp},i} + E_{\mathrm{tr},i} + E_{\mathrm{int},i},$$

$$U_{12}(\sigma_1, \sigma_2) = g_{12} \frac{N_1 N_2}{\sigma_1^3 \sigma_2^3} \int f_1^2\left(\frac{r}{\sigma_1}\right) f_2^2\left(\frac{r}{\sigma_2}\right) d^3r \Rightarrow E_{\mathrm{int},12}. \tag{B21}$$

The "⇒" denotes what the expression reduces to when σ_i takes the equilibrium value in the ground state. $E_{\mathrm{zp},i} = \int \hbar^2/(2m_i)\nabla^2 n_i d^3r$, $E_{\mathrm{tr},i} = \int (1/2) m_i \omega_0^2 r^2 n_i d^3r$, $E_{\mathrm{int},i} = g_{ii} \int n_i^2 d^3r$, and $E_{\mathrm{int},12} = g_{12} \int n_1 n_2 d^3r$ are respectively the zero-point (kinetic), potential, and interaction energies for species i, and the interspecies interaction energy. $n_i = n_i(r) = |\psi_i(r)|^2$. The "$c$" terms like c_{ZP1} are constants and need not be determined explicitly. From the Euler-Lagrange equation, we find $\beta_i = \frac{\dot{\sigma}_i}{\sigma_i}$, and that for σ_i yields

$$\begin{aligned} m_i N_i c_{\mathrm{tr}i} \ddot{\sigma}_i &= -\frac{\partial}{\partial \sigma_i}(U_i + U_{12}) \\ &= -\frac{1}{\sigma_i}\left[-2\frac{c_{\mathrm{ZP,i}}}{\sigma_i^2} + m_i N_i \omega_0^2 \sigma_i^2 c_{\mathrm{tr,i}} - 3\frac{c_{\mathrm{int,i}}}{\sigma_i^3} - g_{12}\frac{N_1 N_2}{\sigma_1^3 \sigma_2^3}\left(3\int f_1^2 f_2^2 d^3r + \int r \frac{\partial f_i^2}{\partial r} f_j^2 d^3r\right)\right]. \end{aligned} \tag{B22}$$

Given the system is in the ground state where $\sigma_i = \sigma_i^{(0)}$ and $\ddot{\sigma}_i = 0$, it leads to the condition

$$-2E_{\mathrm{zp,i}} + 2E_{\mathrm{tr,i}} - 3E_{\mathrm{int,i}} - 3E_{\mathrm{int},12} - g_{12} \int r \frac{\partial n_i}{\partial r} n_j d^3r = 0. \tag{B23}$$

This condition is numerically verified with the solution from the GPE. Directly adding the above equations for $(i, j) = (1, 2)$ and $(i, j) = (2, 1)$ and using integration by part produces

$$-2(E_{\mathrm{zp},1} + E_{\mathrm{zp},2}) + 2(E_{\mathrm{tr},1} + E_{\mathrm{tr},2}) = 3(E_{\mathrm{int},1} + E_{\mathrm{int},12} + E_{\mathrm{int},2}), \tag{B24}$$

which resembles the virial condition for the single-species case. Then, we assume the oscillating amplitude of σ_i is much smaller than their respective equilibrium values and expand the force term in Eq. (B22) up to linear order in $\tilde{\sigma}_i$. The equation of motion is

$$-m_i N_i c_{\mathrm{tr}i} \ddot{\tilde{\sigma}}_i = \tilde{\sigma}_i \frac{\partial^2}{\partial \sigma_i^2}(U_i + U_{12})\bigg|_{\sigma_i = \sigma_i^{(0)}} + \tilde{\sigma}_j \frac{\partial^2 U_{12}}{\partial \sigma_1 \partial \sigma_2}\bigg|_{\sigma_i = \sigma_i^{(0)}}. \tag{B25}$$

We note that we can symbolically rewrite Eq. (B25) as

$$-\begin{pmatrix} \alpha_1 & 0 \\ 0 & \alpha_2 \end{pmatrix}\begin{pmatrix} \ddot{\tilde{\sigma}}_1 \\ \ddot{\tilde{\sigma}}_2 \end{pmatrix} = \begin{pmatrix} \chi_1 & \delta \\ \delta & \chi_2 \end{pmatrix}\begin{pmatrix} \tilde{\sigma}_1 \\ \tilde{\sigma}_2 \end{pmatrix}, \tag{B26}$$

where $\alpha_i \equiv m_i N_i c_{\mathrm{tr},i}$. Explicitly, the symbols represent

$$\left(\sigma_i^{(0)}\right)^2 \chi_i \equiv \sigma_i^2 \frac{\partial^2}{\partial \sigma_i^2}(U_i + U_{12})\bigg|_{\mathrm{equil}} = 6E_{\mathrm{zp},i} + 2E_{\mathrm{tr},i} + 12E_{\mathrm{int},i} + 12E_{\mathrm{int},12} + 8g_{12}\int r \frac{\partial n_i}{\partial r} n_j d^3r + g_{12}\int r^2 \frac{\partial^2 n_i}{\partial r^2} n_j d^3r,$$

$$\sigma_1^{(0)} \sigma_2^{(0)} \delta \equiv \sigma_1 \sigma_2 \frac{\partial^2 U_{12}}{\partial \sigma_1 \partial \sigma_2}\bigg|_{\mathrm{equil}} = g_{12} \int r^2 \frac{\partial n_1}{\partial r}\frac{\partial n_2}{\partial r} d^3r. \tag{B27}$$

Since all the coefficients are known and Eq. (B25) just represents the coupled harmonic oscillators, we can obtain the excitation frequencies in terms of the ground-state density distributions. The eigenfrequencies are

$$\omega^2 = \frac{\chi_1}{2\alpha_1} + \frac{\chi_2}{2\alpha_2} \pm \frac{1}{2}\sqrt{4\frac{\delta^2}{\alpha_1 \alpha_2} + \left(\frac{\chi_1}{\alpha_1} - \frac{\chi_2}{\alpha_2}\right)^2}, \tag{B28}$$

where we see that the frequencies are unchanged if $\alpha_i \to \alpha_i(\sigma_i^{(0)})^2 = 2E_{\mathrm{tr},i}$, $\chi_i \to \chi_i(\sigma_i^{(0)})^2$, and $\delta \to \sigma_1^{(0)}\sigma_2^{(0)}\delta$. Therefore, we can use the expression in Eq. (B27) without the explicit determination of $\sigma_i^{(0)}$. The frequencies obtained by Eq. (B28) using the numerical ground-state distributions from the GPE are consistent with the results from BdGEs for small a_{12}.

b. After hollowing transition

Here, we describe the breathing modes when ^{23}Na has already formed a shell. We employ *Ansätze* similar to that in Ref. [27], with the coupling between the width and the radial center motion of the shell species included. Explicitly, the

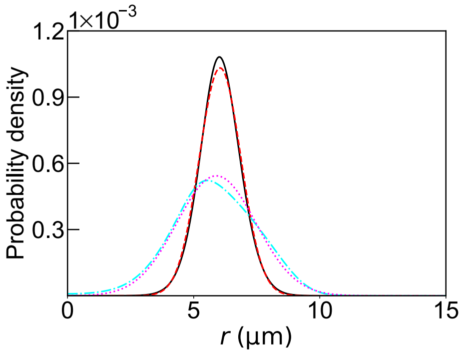

FIG. 10. $a_{12} = 36a_0$, which is beyond the hollowing transition points, for all curves. Black line: BdGEs, $N_1 = 10^3$, $N_2 = 10^5$. Red dashed line: Gaussian *Ansätze*, $N_1 = 10^3$, $N_2 = 10^5$. Aqua dashed-dotted: BdGEs, $N_1 = 10^5$, $N_2 = 7 \times 10^4$. Magenta dotted: Gaussian *Ansätze*, $N_1 = 10^5$, $N_2 = 7 \times 10^4$.

Ansätze are

$$\psi_1(r,t) = \frac{\sqrt{N_1}}{\sqrt{2\pi^{3/2}\sigma_1\left(2r_c^2+\sigma_1^2\right)}} e^{-\frac{1}{2}(\frac{r-r_c}{\sigma_1})^2} e^{\mathbf{i}\beta_0 m_1 r/\hbar + \mathbf{i}\beta_1 m_1 (r-r_c)^2/(2\hbar)},$$

$$\psi_2(r,t) = \frac{\sqrt{N_2}}{\sigma_2^{3/2}} f_2\left(\frac{r}{\sigma_2}\right) e^{\mathbf{i}\beta_2 m_2 r^2/(2\hbar)}, \tag{B29}$$

where $r_c(t)$, $\sigma_1(t)$, $\sigma_2(t)$, $\beta_0(t)$, $\beta_1(t)$, and $\beta_2(t)$ are variational parameters. $r_c(t)$ is a new parameter characterizing the radial center of the ^{23}Na's distribution. The comparison with the sodium density distribution from the GPE and this *Ansatz* is shown in Fig. 10. The velocity field for ^{23}Na is $\beta_0(t)\hat{r} + \beta_1(t)(r - r_c)\hat{r}$, such that β_0 characterizes the radial center's motion. Generally, r_c and σ_1 have complicated coupling. To simplify the situation we assume ^{23}Na forms a thin shell, meaning that [27]

$$r_c \gg \sigma_1, \tag{B30}$$

where σ_1/r_c is an expansion parameter. Indeed, this expansion causes the result in this section to be only valid after the hollowing transition. As a technical remark, we approximate $\mathrm{Erf}(r_c/\sigma_1) \approx 1$ and $e^{-(r_c/\sigma_1)^2} \approx 0$ due to their rapid convergence, where $\mathrm{Erf}(x)$ is the error function. Furthermore, we assume the lengths to oscillate in very small amplitudes to keep harmonic motions, such that the ordering is

$$\left(\frac{\tilde{\sigma}_1}{\sigma_1} \sim \frac{\tilde{r}_c}{r_c}\right) \ll \frac{\sigma_1^2}{r_c^2}, \quad \frac{\tilde{\sigma}_1}{\tilde{r}_c} \sim \frac{\sigma_1}{r_c}, \tag{B31}$$

where $\tilde{\sigma}_1$ is the deviation of σ_1 from its equilibrium value. It means that, up to second order in σ_1/r_c, terms like $\frac{\dot{\sigma}_1}{r_c}\dot{\sigma}_1 = \frac{\dot{\tilde{\sigma}}_1}{r_c}\dot{\tilde{\sigma}}_1$ are discarded. $\tilde{\sigma}_1/\sigma_1 \sim \tilde{r}_c/r_c$ because $\tilde{\sigma}_1/\sigma_1$ needs to be comparable to $\tilde{r}_c/r_c$ for the strong coupling to occur for a thick shell. In the thin shell limit ($\sigma_1 \to 0$), the width is frozen so $\tilde{\sigma}_1 \to 0$.

The Lagrangian is $\mathcal{L} = \mathcal{L}_1 + \mathcal{L}_2 - U_{12}$; up to second order we have

$$\mathcal{L}_1 = -m_1\left[\frac{1}{2}\beta_0^2 + \frac{\sigma_1}{r_c}(\beta_0\beta_1 - \beta_1\dot{r}_c + \dot{\beta}_0)\sigma_1 + \frac{1}{4}\left(1 + \frac{\sigma_1^2}{r_c^2}\right)\beta_1^2\sigma_1^2 + \dot{\beta}_0 r_c + \frac{1}{4}\dot{\beta}_1\sigma_1^2\right] - U_1(r_c, \sigma_1),$$

$$\mathcal{L}_2 = -\left[\frac{1}{2}m_2 N_2 \sigma_2^2 c_{\mathrm{tr},2}\left(\dot{\beta}_2 + \beta_2^2\right) + U_2(\sigma_2)\right]. \tag{B32}$$

In practical calculation, for terms involving β_i and its derivative, we keep up to fourth order in σ_1/r_c. Because $\dot{r}_c/\dot{\sigma}_1 \sim r_c/\sigma_1$, a term like $\frac{\sigma_1^3}{r_c^3}\frac{\dot{r}_c}{\dot{\sigma}_1}$ is in fact a second-order term. The terms $U_i \Rightarrow E_{\mathrm{zp},i} + E_{\mathrm{tr},i} + E_{\mathrm{int},i}$ and $U_{12} \Rightarrow E_{\mathrm{int},12}$ in the ground state. Since we assume an explicit form for $\psi_1(r,t)$, U_1 are explicit functions of σ_1 and r_c, and we can determine their equilibrium values from the zero-point and potential energies. For the velocity field parameters, we find

$$\beta_0 = \left(1 - \frac{\sigma_1^2}{r_c^2}\right)\dot{r}_c + \frac{\sigma_1}{r_c}\dot{\sigma}_1,\ \beta_1 = \left(1 - \frac{\sigma_1^2}{r_c^2}\right)\frac{\dot{\sigma}_1}{\sigma_1} + \frac{\sigma_1^2}{r_c^2}\frac{\dot{r}_c}{r_c}, \tag{B33}$$

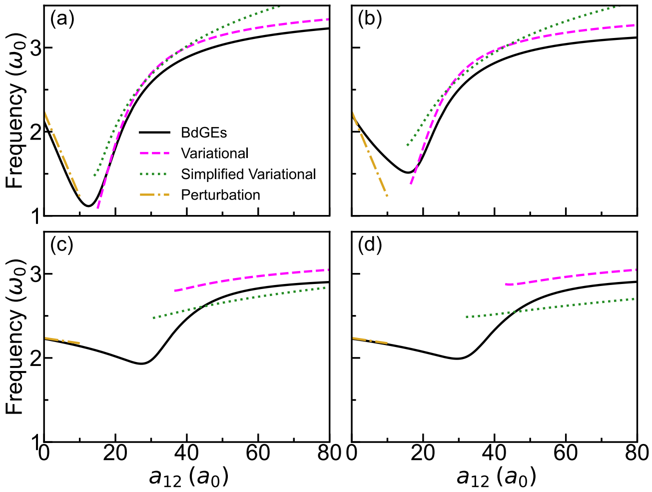

FIG. 11. The theoretic prediction for the out-of-phase mode excitation frequency vs a_{12} for different N_1 and N_2. Results from the BdGEs, variational method, simplified variational method [only look at $r_c(t)$], and perturbation are shown. The perturbation lines for (a) and (b) are $\sqrt{5}\omega_0[1 - g_{12}m_2/(2g_{22}m_1)]$, while for (c) and (d) they are $\sqrt{5}\omega_0[1 - g_{12}m_1/(g_{11}m_2)]$. (a) $N_1 = 10^3$ and $N_2 = 10^5$. At $a_{12} = 0a_0$, the excitation frequency is not $\sqrt{5}\omega_0$ because N_1 is not large enough. (b) $N_1 = 10^4$ and $N_2 = 10^5$. (c) $N_1 = 10^5$ and $N_2 = 10^5$. (d) $N_1 = 10^5$ and $N_2 = 7 \times 10^4$.

which exhibit the coupling between the width and the radial center motions. The equilibrium conditions are

$$
\begin{aligned}
&- N_1\frac{\hbar^2}{2m_1 r_c^2} + 2E_{\mathrm{tr},1} - N_1\frac{5}{2}m_1\omega_0^2\sigma_1^2 - 2E_{\mathrm{int},1} + \frac{3g_{11}N_1^2\sigma_1}{16\sqrt{2}\pi^{3/2}r_c^4} - \left(2 - \frac{\sigma_1^2}{r_c^2}\right)E_{\mathrm{int},12} - g_{12}r_c\int \frac{\partial n_1}{\partial r}n_2 d^3r = 0,\\
&- 2E_{\mathrm{zp},1} + N_1\frac{\hbar^2}{2m_1 r_c^2} + N_1\frac{5}{2}m_1\omega_0^2\sigma_1^2 - E_{\mathrm{int},1} - \frac{3g_{11}N_1^2\sigma_1}{16\sqrt{2}\pi^{3/2}r_c^4} - \left(1 + \frac{\sigma_1^2}{r_c^2}\right)E_{\mathrm{int},12} - g_{12}\int (r - r_c)\frac{\partial n_1}{\partial r}n_2 d^3r = 0, \qquad \text{(B34)}
\end{aligned}
$$

where r_c, σ_1, and σ_2 are meant to be their equillibrium values in the above formula. These conditions are numerically verified after hollowing transition. For the equations of motion, similar to the derivation in the previous section, we apply the Euler-Lagrange equation for σ_i and r_c, and substitute the expression for the velocity field parameters. Then, assuming σ_i and r_c undergo small amplitude oscillations, we linearize the equations and turn them into the form of a generalized eigenvalue problem, where the excitation frequencies are obtained by diagonalization.

As a technical remark, we use the Gaussian *Ansatz* for n_1 instead of the GPE solution in evaluating terms like $\int n_1 n_2 d^3r$ for self-consistency. As the ^{23}Na shell gets thinner with decreasing N_1, the results from the variational method converge to that from BdGEs. However, the variational method cannot capture the trend for very large a_{12} because our *Ansatz* for ^{23}Na in Eq. (B29) does not capture the skewness of the wave function. The skewness is becoming important as g_{12} increases, as we can see from the effective potential $V_{\mathrm{eff}}(r) = \frac{1}{2}m_1\omega_0^2 r^2 + g_{12}n_2(r)$. As g_{12} increases, $V_{\mathrm{eff}}(r)$ turns into a hard wall and a harmonic trap potential, and the actual wave function becomes more skew symmetric. A symmetric Gaussian function either allows a penetration into the hard wall or shifts the radial center to the wrong location.

In Fig. 11, we show the results from the full and simplified variational methods [only $r_c(t)$ in motion] with the ground-state distributions obtained from the GPE for different particle numbers of the species. As expected, the results of the variational method converge to those of the BdGEs as the ^{23}Na shell becomes thinner [from Fig. 11(d) to Fig. 11(a)]. The simplified one also captures the frequency trend. The convergence of the variational method can be improved by taking into account the skewness of the ^{23}Na density profile, but the mathematical difficulty increases.

[1] I. Khalatnikov, Hydrodynamics of solutions of two superfluid liquids, Zh. Eksp. Teor. Fiz. **32**, 653 (1957) [Sov. Phys. JETP **5**, 542 (1957)].

[2] T.-L. Ho and V. B. Shenoy, Binary mixtures of Bose condensates of alkali atoms, Phys. Rev. Lett. **77**, 3276 (1996).

[3] B. D. Esry, C. H. Greene, J. P. Burke, Jr., and J. L. Bohn, Hartree-Fock theory for double condensates, Phys. Rev. Lett. **78**, 3594 (1997).

[4] C. K. Law, H. Pu, N. P. Bigelow, and J. H. Eberly, "Stability signature" in two-species dilute Bose-Einstein condensates, Phys. Rev. Lett. **79**, 3105 (1997).

[5] H. Pu and N. P. Bigelow, Properties of two-species Bose condensates, Phys. Rev. Lett. **80**, 1130 (1998).

[6] H. Pu and N. P. Bigelow, Collective excitations, metastability, and nonlinear response of a trapped two-species Bose-Einstein condensate, Phys. Rev. Lett. **80**, 1134 (1998).

[7] E. Timmermans, Phase separation of Bose-Einstein condensates, Phys. Rev. Lett. **81**, 5718 (1998).

[8] A. Sinatra, P. O. Fedichev, Y. Castin, J. Dalibard, and G. V. Shlyapnikov, Dynamics of two interacting Bose-Einstein condensates, Phys. Rev. Lett. **82**, 251 (1999).

[9] D. S. Hall, M. R. Matthews, J. R. Ensher, C. E. Wieman, and E. A. Cornell, Dynamics of component separation in a binary mixture of Bose-Einstein condensates, Phys. Rev. Lett. **81**, 1539 (1998).

[10] S. B. Papp, J. M. Pino, and C. E. Wieman, Tunable miscibility in a dual-species Bose-Einstein condensate, Phys. Rev. Lett. **101**, 040402 (2008).

[11] G. Modugno, M. Modugno, F. Riboli, G. Roati, and M. Inguscio, Two atomic species superfluid, Phys. Rev. Lett. **89**, 190404 (2002).

[12] D. J. McCarron, H. W. Cho, D. L. Jenkin, M. P. Köppinger, and S. L. Cornish, Dual-species Bose-Einstein condensate of ^{87}Rb and ^{133}Cs, Phys. Rev. A **84**, 011603 (2011).

[13] A. Lercher, T. Takekoshi, M. Debatin, B. Schuster, R. Rameshan, F. Ferlaino, R. Grimm, and H. C. Nägerl, Production of a dual-species Bose-Einstein condensate of Rb and Cs atoms, Eur. Phys. J. D **65**, 3 (2011).

[14] L. Wacker, N. B. Jørgensen, D. Birkmose, R. Horchani, W. Ertmer, C. Klempt, N. Winter, J. Sherson, and J. J. Arlt, Tunable dual-species Bose-Einstein condensates of ^{39}K and ^{87}Rb, Phys. Rev. A **92**, 053602 (2015).

[15] F. Wang, X. Li, D. Xiong, and D. Wang, A double species ^{23}Na and ^{87}Rb Bose-Einstein condensate with tunable miscibility via an interspecies Feshbach resonance, J. Phys. B **49**, 015302 (2016).

[16] P. Maddaloni, M. Modugno, C. Fort, F. Minardi, and M. Inguscio, Collective oscillations of two colliding Bose-Einstein condensates, Phys. Rev. Lett. **85**, 2413 (2000).

[17] L. Cavicchioli, C. Fort, M. Modugno, F. Minardi, and A. Burchianti, Dipole dynamics of an interacting bosonic mixture, Phys. Rev. Res. **4**, 043068 (2022).

[18] D. S. Petrov, Quantum mechanical stabilization of a collapsing Bose-Bose mixture, Phys. Rev. Lett. **115**, 155302 (2015).

[19] C. R. Cabrera, L. Tanzi, J. Sanz, B. Naylor, P. Thomas, P. Cheiney, and L. Tarrue, Quantum liquid droplets in a mixture of Bose-Einstein condensates, Science **359**, 301 (2018).

[20] G. Semeghini, G. Ferioli, L. Masi, C. Mazzinghi, L. Wolswijk, F. Minardi, M. Modugno, G. Modugno, M. Inguscio, and M. Fattori, Self-bound quantum droplets of atomic mixtures in free space, Phys. Rev. Lett. **120**, 235301 (2018).

[21] C. D'Errico, A. Burchianti, M. Prevedelli, L. Salasnich, F. Ancilotto, M. Modugno, F. Minardi, and C. Fort, Observation of quantum droplets in a heteronuclear bosonic mixture, Phys. Rev. Res. **1**, 033155 (2019).

[22] Z. Guo, F. Jia, L. Li, Y. Ma, J. M. Hutson, X. Cui, and D. Wang, Lee-Huang-Yang effects in the ultracold mixture of ^{23}Na and ^{87}Rb with attractive interspecies interactions, Phys. Rev. Res. **3**, 033247 (2021).

[23] G. Thalhammer, G. Barontini, L. De Sarlo, J. Catani, F. Minardi, and M. Inguscio, Double species Bose-Einstein condensate with tunable interspecies interactions, Phys. Rev. Lett. **100**, 210402 (2008).

[24] F. Jia, Z. Huang, L. Qiu, R. Zhou, Y. Yan, and D. Wang, Expansion dynamics of a shell-shaped Bose-Einstein condensate, Phys. Rev. Lett. **129**, 243402 (2022).

[25] A. Wolf, P. Boegel, M. Meister, A. Balaž, N. Gaaloul, and M. A. Efremov, Shell-shaped Bose-Einstein condensates based on dual-species mixtures, Phys. Rev. A **106**, 013309 (2022).

[26] A. Tononi and L. Salasnich, Shell-shaped atomic gases, Phys. Rep. **1072**, 1 (2024).

[27] C. Lannert, T.-C. Wei, and S. Vishveshwara, Dynamics of condensate shells: Collective modes and expansion, Phys. Rev. A **75**, 013611 (2007).

[28] A. Tononi, F. Cinti, and L. Salasnich, Quantum bubbles in microgravity, Phys. Rev. Lett. **125**, 010402 (2020).

[29] K. Padavić, K. Sun, C. Lannert, and S. Vishveshwara, Vortex-antivortex physics in shell-shaped Bose-Einstein condensates, Phys. Rev. A **102**, 043305 (2020).

[30] R. A. Carollo, D. C. Aveline, B. Rhyno, S. Vishveshwara, C. Lannert, J. D. Murphree, E. R. Elliott, J. R. Williams, R. J. Thompson, and N. Lundblad, Observation of ultracold atomic bubbles in orbital microgravity, Nature (London) **606**, 281 (2022).

[31] K. Padavić, K. Sun, C. Lannert, and S. Vishveshwara, Physics of hollow Bose-Einstein condensates, Europhys. Lett. **120**, 20004 (2017).

[32] K. Sun, K. Padavić, F. Yang, S. Vishveshwara, and C. Lannert, Static and dynamic properties of shell-shaped condensates, Phys. Rev. A **98**, 013609 (2018).

[33] M. S. Safronova, B. Arora, and C. W. Clark, Frequency-dependent polarizabilities of alkali-metal atoms from ultraviolet through infrared spectral regions, Phys. Rev. A **73**, 022505 (2006).

[34] Z. Guo, F. Jia, B. Zhu, L. Li, J. M. Hutson, and D. Wang, Improved characterization of Feshbach resonances and interaction potentials between ^{23}Na and ^{87}Rb atoms, Phys. Rev. A **105**, 023313 (2022).

[35] S. Knoop, T. Schuster, R. Scelle, A. Trautmann, J. Appmeier, M. K. Oberthaler, E. Tiesinga, and E. Tiemann, Feshbach spectroscopy and analysis of the interaction potentials of ultracold sodium, Phys. Rev. A **83**, 042704 (2011).

[36] E. G. M. van Kempen, S. J. J. M. F. Kokkelmans, D. J. Heinzen, and B. J. Verhaar, Interisotope determination of ultracold rubidium interactions from three high-precision experiments, Phys. Rev. Lett. **88**, 093201 (2002).

[37] D. S. Lobser, A. E. S. Barentine, E. A. Cornell, and H. J. Lewandowski, Observation of a persistent non-equilibrium state in cold atoms, Nat. Phys. **11**, 1009 (2015).

[38] F. Jia, Z. Guo, L. Li, and D. Wang, Detection of NaRb Feshbach molecules by photodissociation, Phys. Rev. A **102**, 043327 (2020).

[39] C. J. Pethick and H. Smith, *Bose-Einstein Condensation in Dilute Gases* (Cambridge University Press, New York, 2008).

[40] M. Scherer, B. Lücke, J. Peise, O. Topic, G. Gebreyesus, F. Deuretzbacher, W. Ertmer, L. Santos, C. Klempt, and J. J. Arlt, Spontaneous symmetry breaking in spinor Bose-Einstein condensates, Phys. Rev. A **88**, 053624 (2013).

[41] J. Sanz, A. Frölian, C. S. Chisholm, C. R. Cabrera, and L. Tarruell, Interaction control and bright solitons in coherently coupled Bose-Einstein condensates, Phys. Rev. Lett. **128**, 013201 (2022).

[42] C. Pethick and H. Smith, *Bose-Einstein Condensation in Dilute Gases*, 2nd ed. (Cambridge University Press, New York, 2008).